

# Over-constrained Gravitational Lens Models and the Hubble Constant

C. S. Kochanek<sup>1,2</sup>

<sup>1</sup> *Department of Astronomy, The Ohio State University, 140 West 18th Avenue, Columbus OH 43210*

<sup>2</sup> *Center for Cosmology and AstroParticle Physics, The Ohio State University, 191 W. Woodruff Avenue, Columbus OH 43210*

14 November 2019

## ABSTRACT

It is well known that measurements of  $H_0$  from gravitational lens time delays scale as  $H_0 \propto 1 - \kappa_E$  where  $\kappa_E$  is the mean convergence at the Einstein radius  $R_E$  but that all available lens data other than the delays provide no direct constraints on  $\kappa_E$ . The properties of the radial mass distribution constrained by lens data are  $R_E$  and the dimensionless quantity  $\xi = R_E \alpha''(R_E)/(1 - \kappa_E)$  where  $\alpha''(R_E)$  is the second derivative of the deflection profile at  $R_E$ . Lens models with too few degrees of freedom, like power law models with densities  $\rho \propto r^{-n}$ , have a one-to-one correspondence between  $\xi$  and  $\kappa_E$  (for a power law model,  $\xi = 2(n - 2)$  and  $\kappa_E = (3 - n)/2 = (2 - \xi)/4$ ). This means that highly constrained lens models with few parameters quickly lead to very precise but inaccurate estimates of  $\kappa_E$  and hence  $H_0$ . Based on experiments with a broad range of plausible dark matter halo models, it is unlikely that any current estimates of  $H_0$  from gravitational lens time delays are more accurate than  $\sim 10\%$ , regardless of the reported precision.

**Key words:** gravitational lensing: strong – cosmological parameters – distance scale

## 1 INTRODUCTION

Refsdal (1964) pointed out that the time delays between multiple images in a gravitational lens could be used to determine the Hubble constant. There was a long delay before the discovery of the first lensed quasar (Walsh et al. 1979) and then considerable controversy over the measurement of the first time delay (Schild (1990) versus Press et al. (1992), resolved in favor of the former by Kundić et al. (1997)). The measurement of delays is now routine (e.g., Bonvin et al. 2019, Courbin et al. 2018, Bonvin et al. 2017, recently) and the estimates are generally robust (e.g., Liao et al. 2015). The challenge lies in their cosmological interpretation. Individual lenses yield estimates of  $H_0$  with reported precisions of 4-10% (see Table 1) with higher precisions depending on averaging the estimates from large numbers of lenses. The present state of the art comes from the H0LiCOW collaboration, who report a 2.4% measurement of  $H_0$  using six gravitational lenses (Wong et al. 2019).

The time delay  $\Delta t$  in a lens is roughly proportional to  $H_0^{-1}(1 - \kappa_E)$  where  $\kappa_E$  is the mean convergence (dimensionless surface density)<sup>1</sup> at the Einstein ra-

dius  $R_E$  (Kochanek 2002). Unfortunately, no gravitational lens observable other than the time delay directly constrains  $\kappa_E$  (see, e.g., Gorenstein et al. 1988, Kochanek 2002, Kochanek 2006, Schneider, & Sluse 2013, Wertz et al. 2018, Sonnenfeld 2018), so some additional constraint on the mass distribution is required to determine  $H_0$  from a time delay. It was quickly realized that stellar dynamical measurements, usually just meaning the central velocity dispersion, could provide this constraint (e.g., Grogin, & Narayan 1996, Romanowsky, & Kochanek 1999, Treu, & Koopmans 2002).

If we explore simple lens models constrained by a stellar velocity dispersion  $\sigma_*$ , we find that the fractional uncertainty in  $H_0$  is roughly equal to the fractional uncertainty in  $\sigma_*^2$ . Since the reported uncertainties in  $\sigma_*$  for the H0LiCOW lenses range from 6-10% (see Table 1),  $H_0$  should only be constrained to 12-20%. The  $H_0$  uncertainties reported by H0LiCOW of only 4-10% (also Table 1) are, however, far smaller even after including all other sources of uncertainty in the models (e.g., time delays, the local environment, etc.). This means that the constraints on  $\kappa_E$  and thus  $H_0$  must be coming from the lensing constraints on the mass model rather than the stellar dynamical constraints. In fact, the uncertainties in  $H_0$  are so small compared to those in  $\sigma_*$ , that the stellar dynamical measurements must be making almost no contribution to the overall estimate of  $H_0$ .

As already noted, lensing data cannot determine  $\kappa_E$  –

<sup>1</sup> To be more precise, is proportional to  $1 - \langle \kappa \rangle$  where  $\langle \kappa \rangle$  is the mean surface density in the annulus bounded by the lensed images.

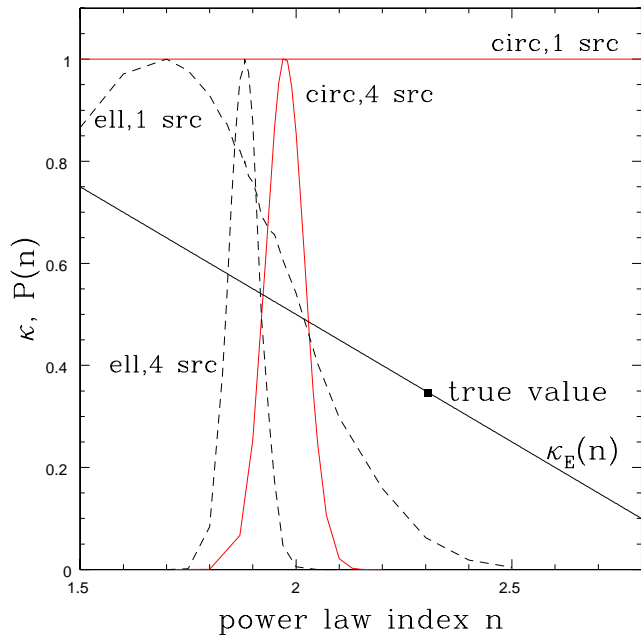


**Figure 1.** Probability of the power law index  $n$  for a Hernquist (1990) model lens with an Einstein radius of  $R_E = 1.3s$  for circular (red, solid) and ellipsoidal (black, dashed) models fitting either one source producing two images (“1 src”) or four sources producing 12 images (“4 src”). For the circular lens, matching the values of  $\xi$  predicts that the best fit power law model should have  $n = 2$ . The solid line shows the dependence of the convergence at the Einstein radius  $\kappa_E(n)$  on the power law index, where the point labeled “true value” is the correct value for the input model.

it is a fundamental degeneracy in the physics of gravitational lensing. Lens models determine  $\kappa_E$  only because the mathematical structure of any density model implies a relationship between the aspects of the model constrained by lens data and the surface density at the Einstein ring. If the density model has too few degrees of freedom compared to the number of lensing constraints, then one quickly obtains a very precise, but likely inaccurate, constraint on  $\kappa_E$  and  $H_0$ . Since the errors are systematic rather than random, there is also no reason to believe that they are reduced by averaging over multiple systems.

Most of these points have been made previously (e.g., Kochanek 2006, Schneider, & Sluse 2013, Xu et al. 2016, Unruh et al. 2017, Sonnenfeld 2018). Here we make these arguments using a different set of analytic results and numerical experiments, which clearly show that the simple density models presently used for most inferences about  $H_0$  from gravitational lens time delays suffer from these problems and become increasingly unreliable as the reported precision becomes smaller than  $\sim 10\%$ . The arguments are presented in §2, and we summarize the results in §3.

## 2 THE ROLE OF PARAMETERS IN THE MASS MODEL

H0LiCOW basically uses two mass models for the lenses. The first model is a simple power law producing a deflection angle of  $\alpha(\theta) = b^{n-1}\theta^{2-n}$ . The model has two parameters,

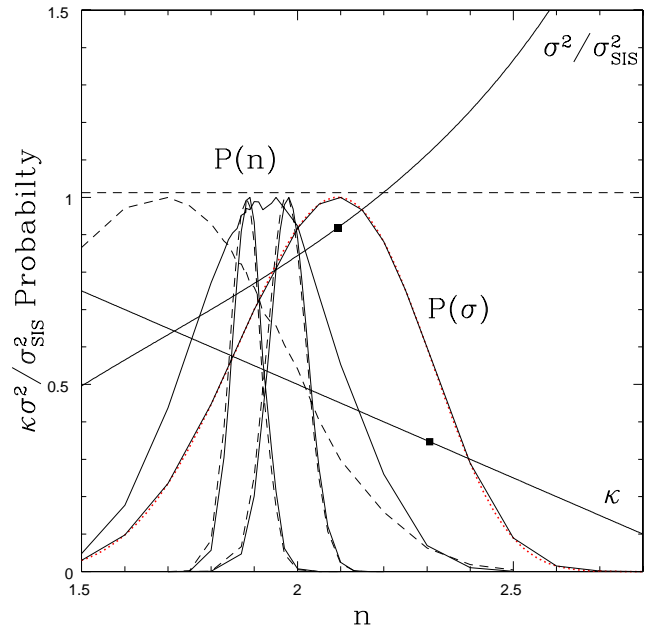


**Figure 2.** Changes in the probability distributions for  $n$  from Fig. 1 after adding a 10% estimate of the velocity dispersion centered on the true value. The dashed curves are the probability distributions from Fig. 1 and the solid curves are the probability distributions including the dynamical constraint. The  $\sigma^2/\sigma_{\text{SIS}}^2$  curve shows the dependence of the velocity dispersion inside the aperture  $R < s$  compared to the velocity dispersion of an SIS lens model.

the Einstein radius  $b$  and the power-law index  $n$  where  $n = 2$  is the SIS model. The second model combines the photometric model of the lens galaxy with a Navarro et al. (1997) NFW profile

$$\rho \propto \frac{1}{r(a+r)^2} \quad (1)$$

for the dark matter halo. In theory, this model has three parameters, a mass to light ratio for the stellar profile, a density normalization for the NFW profile and its scale length  $a$ . In practice, the scale length is constrained by a fairly strong prior to vary by only 10-15%, which effectively makes this a two parameter model as well.

In this section we first review the basic problem that lensing data mathematically cannot determine the surface density  $\kappa_E$  needed to determine  $H_0$  and derive the property of lens models that lens data does constrain. Next we illustrate the problem with a specific example of how mass models with small numbers of parameters can lead to increasingly precise but inaccurate estimates of  $\kappa_E$ . Finally, we show that a range of plausible models for dark matter halos when modeled using the H0LiCOW mass distributions commonly have fractional systematic errors in  $H_0$  of 10% or more.

### 2.1 What Do Lens Models Measure?

We start by reviewing the basic problem. Consider a power law model for circular lens with two images at  $r_1$  and  $-r_2$

**Table 1.** H0LiCOW Lenses

Lens	$\sigma_*$ (km/s)	$H_0$ (km/s/Mpc)	References
HE0435–1223	$222 \pm 15$ (7%)	$73 \pm 6$ (8%)	Wong et al. (2017)
PG 1115+080	$281 \pm 25$ (9%)	$83 \pm 8$ (10%)	Tonry (1998), Chen et al. (2019)
RXJ1131–1231	$323 \pm 20$ (6%)	$80 \pm 6$ (8%)	Suyu et al. (2013)
SDSS 1206+4332	$290 \pm 30$ (10%)	$69 \pm 4$ (6%)	Agnello et al. (2016), Birrer et al. (2019)
B1608+656	$260 \pm 15$ (6%)	$71 \pm 3$ (4%)	Suyu et al. (2010)
WFI2033–4723	$250 \pm 19$ (8%)	$72 \pm 4$ (6%)	Rusu et al. (2019)

( $r_1 \leq r_2$ ). The lens equations require that

$$r_1 - b^{n-1} r_1^{2-n} = -r_2 + b^{n-1} r_2^{2-n}. \quad (2)$$

We can then solve for the Einstein radius,

$$b^{n-1} = \frac{r_1 + r_2}{r_1^{2-n} + r_2^{2-n}}. \quad (3)$$

Not surprisingly, with only one constraint, a solution can be found for any power law index. If we have an additional set of images at  $r_3$  and  $-r_4$  ( $r_4 \leq r_3$  and  $r_2 \leq r_4 \leq r_3 \leq r_1$ ), then there is a unique solution from solving the transcendental equations

$$\frac{r_1 + r_2}{r_1^{2-n} + r_2^{2-n}} = \frac{r_3 + r_4}{r_3^{2-n} + r_4^{2-n}} \quad (4)$$

for the power law index. Because the model has only two parameters, the mass distribution is now exactly defined everywhere up to the uncertainties in the position measurements. In particular, the convergence at the Einstein ring is now forced to be  $\kappa_E = (3 - n)/2$  which in turn forces a particular value for  $H_0$  given a time delay. The mass distribution away from the Einstein ring is also full specified, eliminating any important constraint from the dynamical data because the fractional uncertainties in lensing constraints are generally far smaller than the fractional uncertainties in velocity dispersions.

There are, however, two fundamental problems. First, as noted in the introduction, whatever the available lensing constraints, the one quantity they do not directly constrain is the mean surface density needed to convert a time delay into  $H_0$ . The conversion of the lensing constraints into a value of  $\kappa_E$  is entirely set by the functional form of the mass model and its flexibility. Second, the lens geometry has absolutely no information on the mass distribution inside or outside the annulus encompassing the lens images – the exactly determined mass distribution for these regions is purely an extrapolation set by the functional form of the mass model.

These two points are also easily demonstrated non-parametrically (see Kochanek 2002, Kochanek 2006). Let the mass of the lens between two radii be

$$m(r_1, r_2) = 2 \int_{r_1}^{r_2} u du \kappa(u) \quad (5)$$

where  $\kappa(r)$  is the convergence (surface density) profile of the lens. The deflection angle is then  $\alpha(r) = r^{-1} m(0, r)$  and the lens equations require that

$$r_1 - r_1^{-1} m(0, r_1) = -r_2 + r_2^{-1} m(0, r_2). \quad (6)$$

Now  $m(0, r_1) = m(0, r_2) + m(r_2, r_1)$ , so

$$m(0, r_2) = r_1 r_2 - \langle \kappa \rangle_{21} r_2 (r_1 - r_2), \quad (7)$$

where

$$\langle \kappa \rangle_{ij} = \frac{2}{r_j^2 - r_i^2} \int_{r_i}^{r_j} u du \kappa(u) \quad (8)$$

is the mean convergence in the annulus bounded by  $r_1$  and  $r_2$ . For a thin annulus, the Einstein radius is  $R_E^2 = r_1 r_2$  independent of the surface density, and the mean surface density is the quantity that determines the  $H_0$  given the time delay since  $H_0 \propto 1 - \langle \kappa \rangle_{21}$ . Stellar dynamics essentially provides an independent constraint on  $m(0, r_2)$ , thereby allowing an estimate of  $\langle \kappa \rangle_{21}$  and hence  $H_0$ .

Adding additional lensing constraints does nothing to remove the degeneracy. Suppose  $r_1$  and  $r_2$  bound the region containing lensed images, and we again add an additional pair of lensed images with  $r_2 < r_4 < r_3 < r_1$ . There is now a second constraint equation like Eqn. 6. The non-parametric parameters of the model are now  $m(0, r_2)$ ,  $\langle \kappa \rangle_{24}$ ,  $\langle \kappa \rangle_{43}$  and  $\langle \kappa \rangle_{31}$ , leaving us with four parameters to be constrained by two equations. Viewed as a non-parametric model, the number of parameters expands faster than the number of constraints and the  $H_0$  degeneracy problem cannot be eliminated no matter how many additional pairs of lensed images are added.

The annulus encompassing the lensed images of the quasar and its host is typically rather narrow, so using a simple functional form to describe the mass distribution in this annulus is likely quite reasonable. The problems are (1) that the constraints only apply over the annulus containing the lensed images – any prediction of the mass distribution beyond the annulus is purely an extrapolation, and (2) that they cannot constrain the quantity  $\kappa_E$  needed to determine  $H_0$ . We can illustrate this by first determining what property of a lens is constrained by the data, and then by constructing a model where two radically different radial mass distributions and predictions for  $H_0$  are essentially indistinguishable using lens data.

Suppose we locally expand the deflection angle as a Taylor series near the Einstein radius,  $R_E$ ,

$$\alpha(r) \simeq R_E + 2(\kappa_E - 1)(r - R_E) + \frac{1}{2} \alpha_E'' (r - R_E)^2 \quad (9)$$

where  $\kappa_E$  is the convergence and  $\alpha_E''$  is the second derivative of the deflection profile at  $R_E$ . The lens equation for a source at radius  $\beta$  is then

$$\beta = -2(\kappa_E - 1)(r - R_E) + \frac{1}{2} \alpha_E'' (r - R_E)^2. \quad (10)$$

for one image and with the signs flipped on the right side of the equation for the other image. We can divide both sides

by  $1 - \kappa_E$ , to get

$$\hat{\beta} = 2(r - R_E) + \frac{1}{2}\hat{\alpha}_E''(r - R_E)^2. \quad (11)$$

where  $\hat{\beta} = \beta/(1 - \kappa_E)$  and  $\hat{\alpha}_E'' = \alpha_E''/(1 - \kappa_E)$ . Since the source position  $\beta$  is not an observable, Eqn. 11 means that for images near the Einstein ring, lens models determine  $\hat{\alpha}_E''$  and two lens models are indistinguishable if they have the same  $\hat{\alpha}_E''$ . Alternatively, we can introduce the dimensionless quantity

$$\xi = R_E \hat{\alpha}_E'' = \frac{R_E \alpha_E''(R_E)}{1 - \kappa_E} \quad (12)$$

as the second property of the radial mass distribution after  $R_E$  that can be well-constrained by lens data. Because the uncertainties in  $R_E$  are generally small, the uncertainties in  $\xi$  will be dominated by the uncertainties in  $\hat{\alpha}_E''$ .

Many previous studies have found that lens models modeled as a power law with  $\rho \propto r^{-n}$  favor logarithmic slopes  $n \simeq 2$  close to the  $n = 2$  slope of an isothermal sphere (e.g., Rusin, & Kochanek 2005, Gavazzi et al. 2007, Koopmans et al. 2009, Auger et al. 2010, Bolton et al. 2012). This does not mean that the typical slope of the density distribution on the scale of the Einstein radius has  $n \simeq 2$ . Instead, there is a one-to-one relation that  $\xi = 2(n - 2)$  for the power-law models and the true physical constraint implied by finding  $n \simeq 2$  is that  $\xi \simeq 0$ . It is again important to emphasize that lens models do not determine  $\kappa_E$ , the quantity needed to estimate  $H_0$ . The functional form chosen for the mass model implies some value of  $\kappa_E$  given the value of  $\xi$ , but a different mass model will lead to a different value of  $\kappa_E$  for the same value of  $\xi$ . For the power law models,  $\kappa_E = (3 - n)/2 = (2 - \xi)/4$ , with  $\kappa_E = 1/2$  for  $n = 2$  or  $\xi = 0$ . However, a different mass model will predict a different value of  $\kappa_E$  for the same value of  $\xi$ .

## 2.2 A Demonstration of the Problem

Consider the Hernquist (1990) model,

$$\rho \propto \frac{1}{r(s+r)^3}, \quad (13)$$

where the scale radius is related to the effective radius by  $s \simeq 0.55R_e$ . For a Hernquist (1990) model lens, the value of  $\xi$  depends on the position of the Einstein radius relative to the break radius  $R_E/s$ , and  $\xi = 0$  for  $R_E/s \simeq 1.3$  where  $\kappa_E \simeq 0.35$  is the convergence. If we model this lens as a power law, we should find that  $n \simeq 2$  with  $\kappa_E \simeq 0.5$  as the convergence. This means that the power law lens model will produce a fractional error in  $H_0$  of  $f = H_{true}/H_{model} - 1 \simeq 30\%$ .

Figure 1 shows a sequence of four cases fitting this example of a Hernquist (1990) lens model with a power law model. We ignore the generation of faint third images by the Hernquist (1990) model and the flux ratios of the images. For computing a goodness of fit, we assume astrometric uncertainties of  $0.003s$  for the image and lens positions and no constraints on the ellipticity of the lens or the external shear for the ellipsoidal models. The shear and ellipticity parameters remain reasonable without additional constraints. We fit the fake data using `lensmodel` (Keeton 2001, Keeton 2011) with the  $\chi^2$  goodness of fit computed on the image plane.

We first considered two circular lens models. In the first, we place one image at  $1.1R_E$ , which has a second image at  $-0.89998R_E$ . Note that the image separation of  $1.9998R_E$  is essentially indistinguishable from the  $2R_E$  that would be produced by an SIS model. As seen in Fig. 1, this data can be perfectly fit ( $\chi^2 \equiv 0$ ) independent of the slope of the power law as expected from Eqn. 3. For the second model, we added three additional sources that produced outer images at  $1.05R_E$ ,  $1.2R_E$  and  $1.3R_E$ , respectively. The separations of the three resulting image pairs are also essentially indistinguishable from the  $2R_E$  prediction of an SIS model. If we fit these 4 image pairs, we now find that the model is strongly constrained to have  $n = 2$ , as expected from matching the values of  $\xi$ . The best model ( $n = 1.974$ ) is still a perfect fit with  $\chi^2 = 0.015$  for three degrees of freedom. The surface density at the Einstein ring implied by the model is, however, completely wrong, leading to a 30% error in  $H_0$ . Adding more lensing constraints will never solve the problem – the  $\chi^2$  distribution will simply steadily narrow around  $n \simeq 2$  with smaller and smaller uncertainties in both  $n$  and the implied value of  $\kappa_E$ .

We next considered the same cases but with an ellipsoidal lens in an external shear. We gave the Hernquist (1990) model a surface density axis ratio of  $q = 0.65$  and added an external shear of  $\gamma = 0.05$  at a randomly chosen angle. For the ellipsoidal models, we view  $s$  as the intermediate axis scale length and again normalize the mass so that  $R_E = 1.3s$  (`lensmodel` uses the major axis scale length of  $sq^{-1/2}$  to define the models). We again placed images at  $1.05R_E$ ,  $1.1R_E$ ,  $1.2R_E$  and  $1.3R_E$  and random angles around the lens and then found their companion images. The two images closer to  $R_E$  produced four images, and the two further from  $R_E$  produced two images, so we now have 12 images in total.

We first repeated the fits using the four image system associated with an image at  $1.1R_E$ . We again find a good fit, but at  $n \simeq 1.7$  with  $\chi^2 = 0.004$ . Formally, the model has fewer constraints than parameters ( $-1$  degrees of freedom). The goodness of fit is not independent of  $n$  but clearly selects a preferred range, albeit with relatively large uncertainties. We are confident that this is a consequence of the limited degrees of freedom in the angular structure of the mass model. The density distribution of the Hernquist (1990) model out to  $R_E$  drops more slowly than the  $n = 2$  power-law model, so for the same quadrupole it will have larger higher order multipoles. The power-law models compensate by shifting to lower  $n$ , less centrally concentrated mass distributions. Kochanek (2006) has an extensive discussion on the angular structure of lens models.

If we now add in the other three sources and fit all 12 images, Fig. 1 shows that  $n$  is again tightly constrained but still offset to lower  $n$  than the circular models. The sense of the shift only exacerbates the problems for  $H_0$ , since these models have surface densities at  $R_E$  even higher than the  $n = 2$  SIS model and so are still further from the input model. The best fit models at  $n \simeq 1.88$  are statistically good fits with  $\chi^2 = 3.3$  for 3 degrees of freedom. Adding additional sources producing multiple images simply narrows the probability distribution  $P(n)$ .

Fig. 2 shows the consequences of adding dynamical constraints to the lensing constraints illustrated in Fig. 1. We assume a measured dispersion equal to the true dispersion

for a Hernquist (1990) model inside the aperture  $R < s$  with a 10% uncertainty. Fig. 2 also shows the lensing only probability distributions for  $n$  and the joint lensing+dynamics probability distributions. The circular model with only one two image lens system plus dynamics comes closest to yielding models with the correct value of  $\kappa_E$  since the joint probability distribution is simply the dynamical probability distribution as the lens model imposes no constraint on  $n$ . For the elliptical model with one four image lens system, the dynamical constraint shifts the lensing distribution to be less inconsistent with the correct value of  $\kappa_E$ . For both the circular and ellipsoidal models with 4 sources, the probability distributions are essentially unchanged after adding the dynamical constraint. The lens model is so strongly constrained by the lens data, that the relatively weaker dynamical constraints have little effect.

We tried a broad range of additional numerical examples for a range of mass models. In circular models, the solution always converges to match the  $\xi$  of the input model. In ellipsoidal models with external shear, there are modest shifts from the  $\xi$  of the input model. These experiments explain the puzzle discussed in the introduction. In mass models with few degrees of freedom and very strong lensing constraints, the lens data “pins” the mass model to match the  $\xi$  required by the data. The weaker dynamical constraints then have little effect and estimates of  $H_0$  (i.e.,  $\kappa_E$ ) show little sensitivity to changes in the velocity dispersion. Unfortunately, Figs. 1 and 2 also show that the accuracy of the estimate of  $H_0$  was greatly reduced rather than enhanced by the use of the additional strong lensing constraints.

### 2.3 Consequences

By matching lens models in  $\xi$ , it is now easy to show the consequences of using different mass models in the case of circular lenses. We used an input mass distribution consisting of a de Vaucouleurs (1948) model for the stars plus a dark halo. Qualitatively similar results are obtained if we chose a different density distribution for the stars. We scaled everything by the effective radius  $R_e$  of the deV model and generated models with 0%, 25% or 50% of the mass inside the Einstein radius  $R_E$  coming from the halo. We considered four halo models. The first is simply the NFW model of Eqn. 1. The second is the generalization of the NFW (gNFW) profile

$$\rho \propto \frac{1}{r^\gamma (a^2 + r^2)^{(m-\gamma)/2}} \quad (14)$$

introduced as a lens model by Muñoz et al. (2001). This asymptotically matches generalizations of the NFW model at large and small radii, but the change in structure near the break radius makes the deflection profiles analytic. The case  $\gamma = 1$ ,  $m = 3$  is similar to the NFW model, while  $\gamma = 3/2$ ,  $m = 3$  is similar to the model favored by Moore et al. (1999). The third is the Einasto (1965) profile,

$$\rho \propto \exp \left[ -\frac{2}{\alpha} \left( \left( \frac{r}{a} \right)^\alpha - 1 \right) \right] \quad (15)$$

where  $0.15 \lesssim \alpha \lesssim 0.30$  models may better fit halo simulations than the NFW model (e.g., Merritt et al. 2005, Navarro et al. 2010, Reed et al. 2011). The Einasto (1965) models are most easily treated numerically.

These first three models are for dark matter halos unaffected by baryons, but the actual halo structures of galaxies are modified by the presence and evolution of the baryons. In particular, the baryons adiabatically compress the dark matter orbits as they cool and shrink relative to the dark matter. As a fourth halo model, we use the simple model of adiabatic compression from Blumenthal et al. (1986). We start with an NFW halo and make the final distribution of the baryons a Hernquist (1990) density profile with the same effective radius as the deV model we use for the lens model. We use a NFW concentration of  $c = 10$ , so that the virial radius is  $r_v = ca = 10a$ , and a baryonic mass fraction of 15.7% (Planck Collaboration et al. 2018). We then combine this adiabatically compressed NFW profile with the deV model for the stars, again assuming that either 25% or 50% of the projected mass inside the Einstein ring comes from the halo – we did not force the dark matter fraction implied by the adiabatically compressed model.

Following H0LiCOW, we model the input system using either the power-law mass distribution (“PL”) or the input stellar distribution, here a de Vaucouleurs (1948) model, combined with an NFW model for the halo (“deV+NFW”). We assumed that the effective radii of the two deV models were fixed and identical. With the break radius  $a$  of the NFW model fixed, both mass models have two parameters which we determine by matching the Einstein radius and  $\xi$  of the input model as function of the Einstein radius relative to the effective radius  $R_E/R_e$ . Given the input  $\kappa_{input}$  and model  $\kappa_{model}$  surface densities at the Einstein radius, we can then compute the fractional error in  $H_0$  as

$$f = \frac{H_{true}}{H_{model}} - 1 = \frac{1 - \kappa_{input}}{1 - \kappa_{model}} - 1. \quad (16)$$

This has the sense that the models underestimate (overestimate)  $H_0$  if  $f > 0$  ( $f < 0$ ).

We first consider models where the input halo is NFW using input break radii of  $a/R_E = 5, 10$  and 20. H0LiCOW sets  $a \simeq (58 \pm 8)h^{-1}$  kpc based on the stacked weak lensing analysis of the Sloan ACS lens sample by Gavazzi et al. (2007). This roughly corresponds to  $a/R_e \simeq 10$  for most of the H0LiCOW lenses. Whether from Gavazzi et al. (2007) or simulations (e.g., Bullock et al. (2001) Reed et al. 2011, Dutton, & Macciò 2014),  $a/R_e \simeq 10$  is roughly the correct scale. However, while the 15% uncertainty in  $a$  found by Gavazzi et al. (2007) and used by H0LiCOW may be a realistic estimate of the uncertainty in the mean scale length, it greatly underestimates the plausible range of scale lengths for individual lenses. The lens galaxies have a finite spread in halo mass, and halo concentrations have significant scatter at fixed halo mass (e.g., Dutton, & Macciò 2014). There are further dependencies on the redshifts of formation and observation. Hence, the factor of two range around  $a/R_e = 10$  we use for illustration is relatively realistic even if  $a/R_e = 10$  is the true mean halo scale length of lenses. Figure 3 shows fractional errors from modeling these lenses using either a power law model or deV+NFW models with the same three break radii.

If lenses happen to have deV+NFW mass distributions with  $f_{DM} = 25\%$  and  $a/R_E = 10$ , then the power law models do remarkably well, with fractional errors of only 1-2% for the range of  $R_E/R_e$  spanned by the lenses. However, for any other dark matter fraction or scale length, the frac-

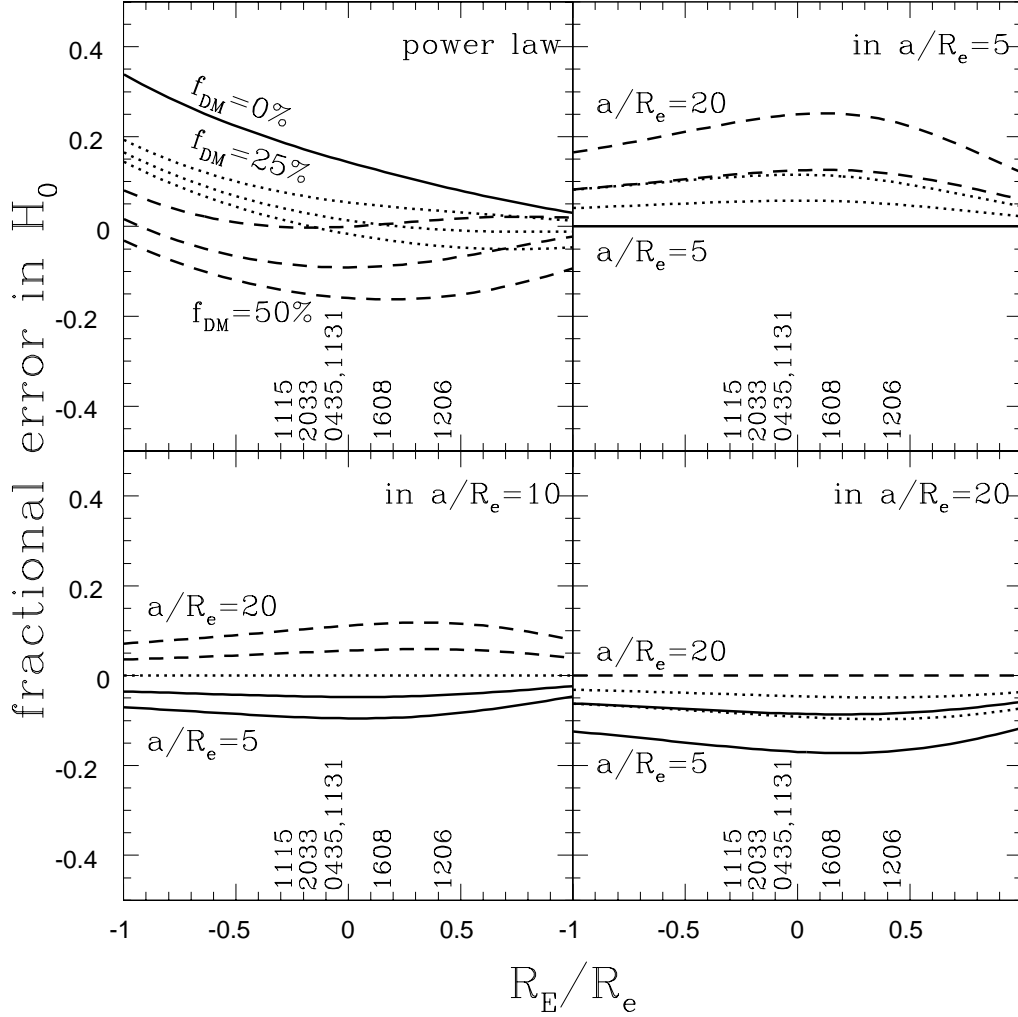


**Figure 3.** Fractional errors in  $H_0$  for an input deV+NFW halo modeled as a power law (top left) or a deV+NFW halo model (other panels). In the power law panel the dark matter fraction is  $f_{DM} = 0\%$  (solid),  $25\%$  (dotted) or  $50\%$  (dashed) for input NFW scale lengths of  $a/R_E = 5$  (top) or  $20$  (bottom). For the NFW panels, the input NFW scale length is  $a/R_E = 5$  (top left) or  $20$  (lower right), and the model NFW scale length is  $a/R_e = 5$  (dotted),  $10$  (solid) or  $20$  (dashed) in each panel. Results are shown for dark matter fractions of  $f_{DM} = 25\%$  or  $50\%$  with larger fractional errors for larger dark matter fractions. When  $f_{DM} = 0\%$  or the input and model NFW scale lengths are the same, the fractional error is zero. The locations of the H0LiCOW lenses in  $R_E/R_e$  are indicated by the lens names.

tional errors quickly exceed 5%. The exact values of the systematic errors found for the power law models are quite sensitive to changing the stellar mass distribution. For example, for this deV+NFW model, the fractional error for  $R_E = 1.3s = 0.72R_e$  is 15% instead of the 30% fractional error we found for the same Einstein radius in the Hernquist (1990)+NFW model of §2.2.

The other three panels of Fig. 3 show the results for the deV+NFW model and the consequences of differences in the NFW break radius. If the input and model break radii match, or there is no dark matter ( $f_{DM} = 0\%$ ), then the lens model can exactly reproduce the input model and the fractional errors are zero. However, if the lens model scale length is greater (less) than the true scale length,  $H_0$  is underestimated (overestimated) with the magnitude of the error increasing with the dark matter fraction. Changing

the stellar distribution, but still using the same stellar mass distribution to both generate and model the lens, seems to have little effect on systematic errors found when modeling the system by the stellar density plus an NFW halo.

Next we consider the gNFW models (Eqn. 14), where we can vary the inner ( $\gamma$ ) and outer ( $m$ ) logarithmic slopes of the profile as well as the scale length  $a$ . Figure 4 shows the results where both the gNFW and NFW profiles have  $a/R_e = 10$ . The first point to note is that even with the same scale length and exponents matching those of the NFW profile ( $\gamma = 1$ ,  $m = 3$ ), there are significant changes in the fractional errors for  $H_0$  whether using the power law or deV+NFW models. As before, the shifts increase as the dark matter fraction increases. Varying the outer slope  $m$  has relatively little effect on the results for the  $2.7 \leq m \leq 3.3$  range shown. Varying the inner slope over the range

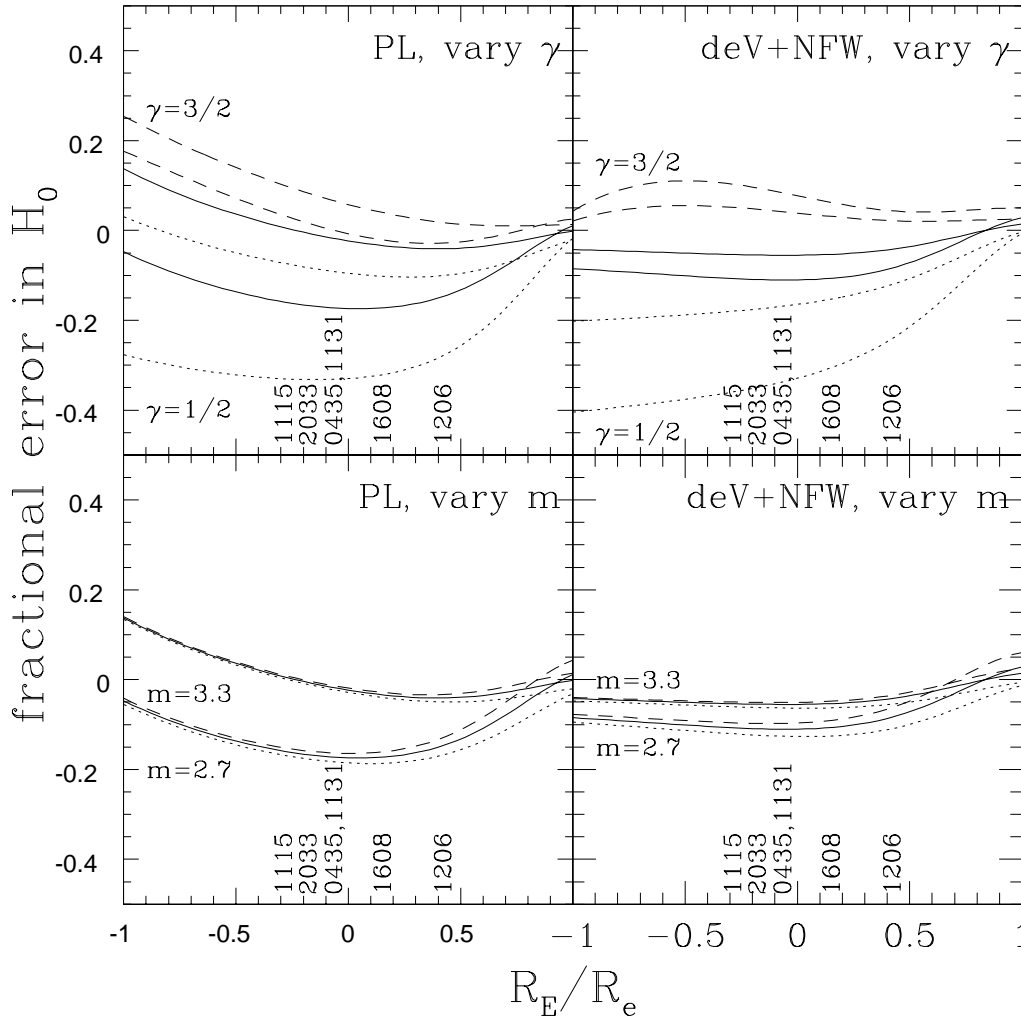


**Figure 4.** Fractional errors in  $H_0$  for an input deV+gNFW halo modeled as a power law (“PL”, left panels) or a deV+NFW halo model (deV+NFW, right panels). In the top panels, the asymptotic slope  $m = 3$  is fixed and the inner density slope exponent of the gNFW model is  $\gamma = 1/2$  (dotted),  $\gamma = 1$  (solid) or  $\gamma = 3/2$  (dashed). In the lower panels, the inner exponent is fixed to  $\gamma = 1$  while the asymptotic slope is  $m = 2.7$  (dotted),  $m = 3$  (solid) and  $m = 3.3$  (dashed). The scale length is fixed to  $a/R_e = 10$  for both the gNFW and NFW models and the dark matter fraction is either  $f_{DM} = 25\%$  or  $50\%$ , with larger fractional errors for larger  $f_{DM}$ .

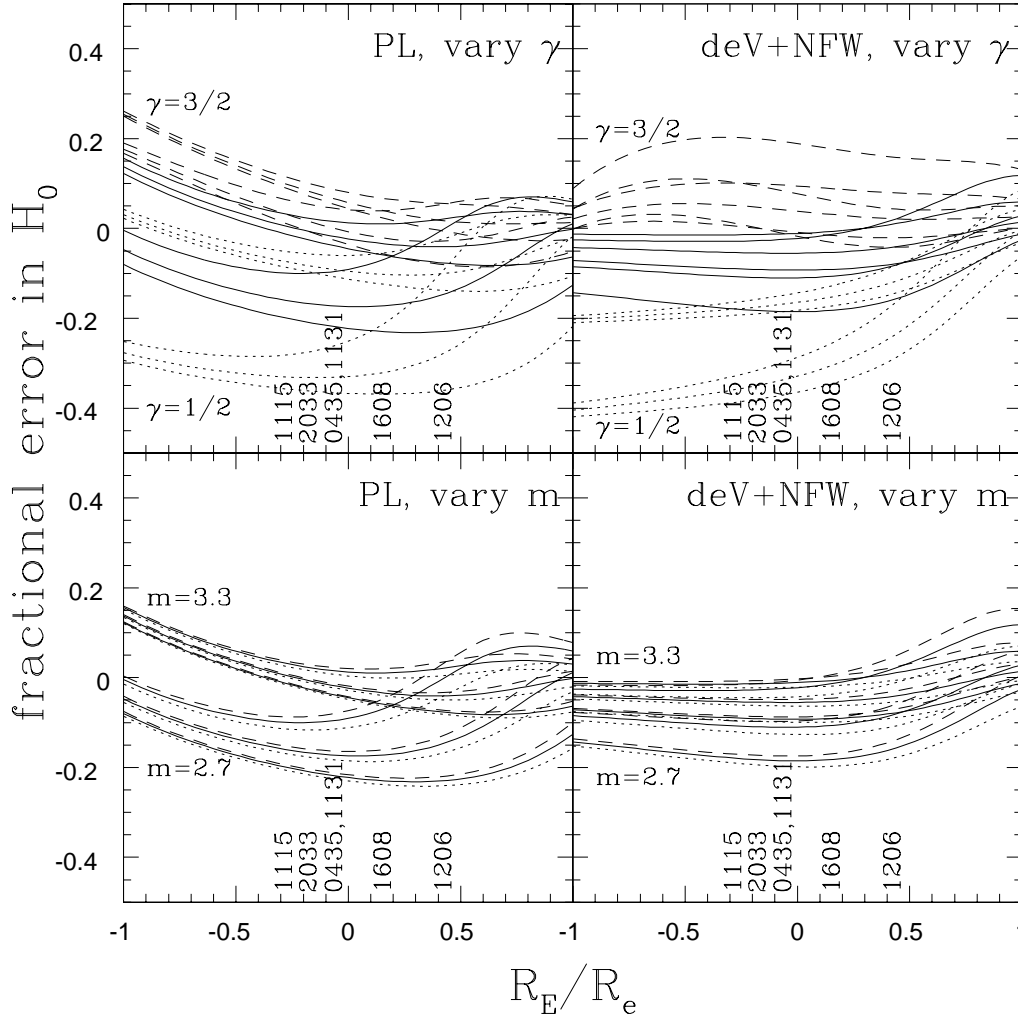
$1/2 \leq \gamma \leq 3/2$  creates quite large shifts, where the models tend to underestimate (overestimate)  $H_0$  as we make the inner profile steeper (shallower). The limit  $\gamma = 3/2$  is the slope favored by Moore et al. (1999). As shown in Fig. 5, changing the scale length  $a$  to  $a/R_e = 5$  or  $a/R_e = 20$  produces significant changes compared to  $a/R_e = 10$  even though we continue to use the same break radius for both the input gNFW mass model and the lens NFW model. We do not show the cases where we allow the two break radii to differ, but this leads to still broader ranges for the fractional errors that are qualitatively similar to the effects for the deV+NFW models in Fig. 3.

Fig. 6 shows the results for the Einasto (1965) halo models with a dark matter fraction of  $f_{DM} = 25\%$ . The fractional errors depend on the parameter  $\alpha$ , shifting towards more positive fractional errors as  $\alpha$  is reduced. As with the other halo models, more compact halos and halos of one scale length modeled by one with a smaller scale length are

also shifted towards more positive fractional errors. The typical scale of the systematic errors for  $f_{DM} = 25\%$  is again of order 10% for reasonable ranges of the model parameters, rising to  $\sim 20\%$  for  $f_{DM} = 50\%$ .

Fig. 7 shows the results for the adiabatically compressed NFW halos with a dark matter fraction of  $f_{DM} = 25\%$ . The adiabatically compressed halos are more centrally concentrated, so it is not surprising that the main qualitative change from the NFW models in Fig. 3 is to shift the fractional errors to larger positive values. The qualitative shifts seen in Fig. 7 are also found if we adiabatically compress the Einasto (1965) profiles and are presumably generic.

So far, we have assumed that the shape of the stellar density distribution is exactly the same in both generating and modeling the lens, leaving only the mass-to-light ratio as a parameter of the lens models. Photometric models of the lens galaxies generally leave small fractional residuals, so if the stellar distributions have constant mass-to-light ratios



**Figure 5.** As in Fig. 4 but adding the results for both models having  $a/R_e = 5$  and 20. The same halo scale length is still used for both input gNFW and model NFW profiles. The spread increases further if we allow the scale lengths to differ as in Fig. 3.

this is likely a safe assumption until pursuing  $\sim 1\%$  fractional uncertainties in  $H_0$ . However, it is routine to find that surface brightness profiles depend on the filter of observation or equivalently that early-type galaxies have color gradients indicative of radial changes in age or metallicity that in turn imply changes in the stellar mass-to-light ratio (see, e.g., the review by Kormendy, & Djorgovski 1989). Thus, as a final experiment, we gave the input stellar mass distribution a gradient in its mass-to-light ratio. We multiplied the input deV density distribution by

$$1 + \mu \left( \frac{R - R_e}{R_e} \right) \quad (17)$$

but modeled the stellar mass distribution using just the input deV density distribution (i.e.  $\mu \equiv 0$ ). For illustration we used  $\mu = \pm 0.2$ , so a 20% change in the mass-to-light ratio per effective radius. We did not worry about the mass-to-light ratio becoming negative for large radii when  $\mu < 0$ , as all that matters is the mass-to-light ratio from the center to  $R_E$ , and the Einstein radii are well inside the radius where the model becomes problematic. As shown in Fig. 8,

modest gradients in the stellar mass-to-light ratio can easily lead to 5-10% systematic errors in estimates of  $H_0$  even if the photometric profile of the lens in some filter is exactly known.

### 3 DISCUSSION

Estimates of  $H_0$  from lens time delays are controlled by the convergence (surface density)  $\kappa_E$  at the Einstein radius  $R_E$ , with  $H_0 \propto 1 - \kappa_E$ . No differential lens data (image separations, flux ratios, etc.) other than the time delays *ever* directly constrains  $\kappa_E$  – it is a fundamental degeneracy in the mathematics of lensing (see, e.g., Gorenstein et al. 1988, Kochanek 2002, Kochanek 2006, Schneider, & Sluse 2013, Wertz et al. 2018). Lens data constrains two properties of the radial mass distribution: (1) the Einstein radius  $R_E$ ; and (2) the dimensionless number  $\xi = R_E \alpha''(R_E)/(1 - \kappa_E)$  where  $\alpha''(R_E)$  is the second derivative of the deflection profile at the Einstein radius. Any lens with constraints from more than one set of lensed images will strongly constrain

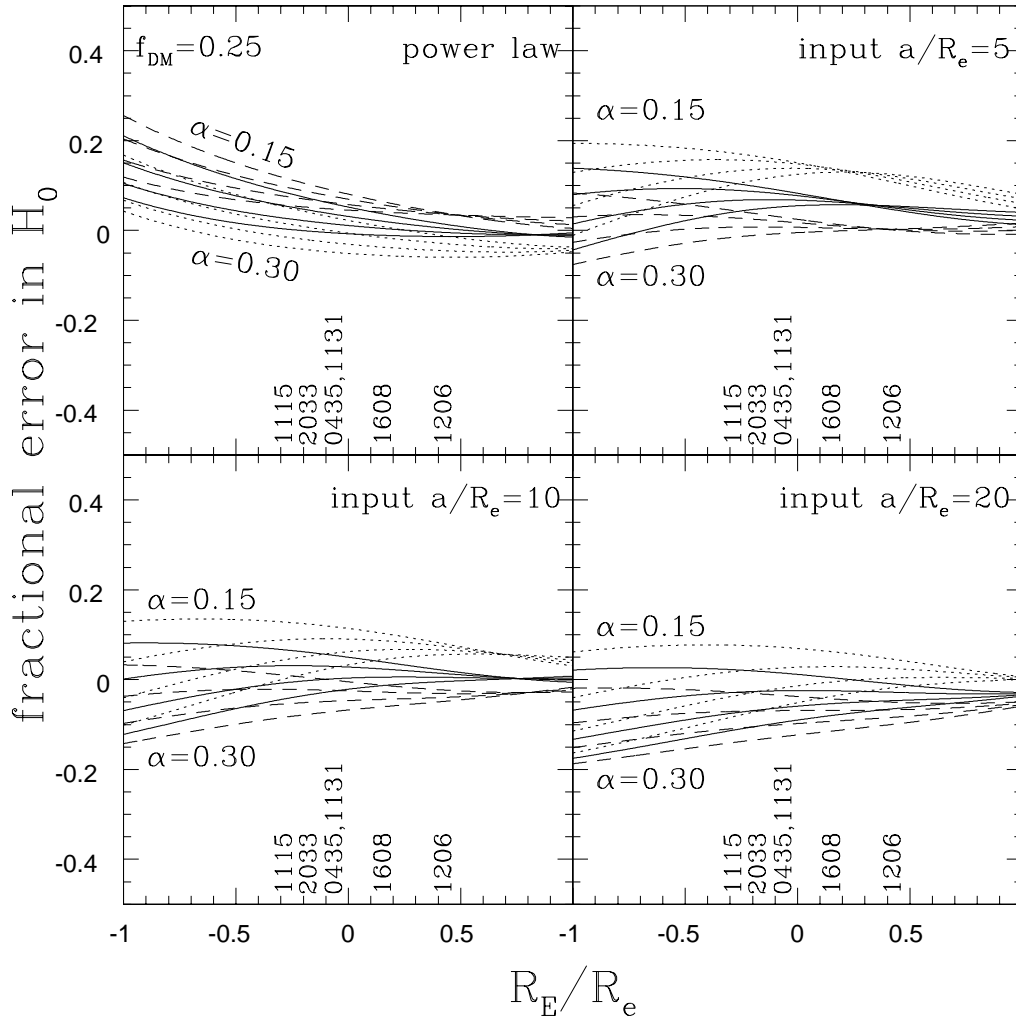


**Figure 6.** Fractional errors in  $H_0$  for deV+Einasto models with  $f_{DM} = 25\%$  and  $\alpha = 0.15, 0.20, 0.25$  and  $0.30$ . The top left panel uses power law models for Einasto halos with  $a/R_e = 5$  (dashed),  $10$  (solid) and  $20$  (dotted). The remaining panels show deV+NFW models applied to Einasto profiles with  $a/R_e = 5$  (top right),  $10$  (lower left) and  $20$  (lower right). The NFW models use  $a/R_e = 5$  (dashed),  $10$  (solid) and  $20$  (dotted).

$R_E$  and  $\xi$ . If the (radial) mass model has only two parameters, this will also lead to tight constraints on  $\kappa_E$  and hence  $H_0$  because the model has no additional degrees of freedom. For example, in power-law lens models with deflection profiles  $\alpha(R) = b^{n-1}R^{2-n}$ ,  $R_E = b$ ,  $\xi = 2(n-2)$  and  $\kappa_E = (3-n)/2 = (2-\xi)/4$ . But the constraint on  $\kappa_E$  is purely dictated by the mathematical structure of the lens model and not by the lens data. We demonstrate this point in detail for a particular model, admittedly chosen to lead to an alarming, 30% fractional error in  $H_0$ .

We carried out an extensive survey of the consequences of using strong lens constraints by simply matching  $R_E$  and  $\xi$  between mass models. For the input models, we considered lenses consisting of a de Vaucouleurs (1948) model combined with a broad range of physically reasonable halo models (the Navarro et al. (1997) NFW model, generalizations of the NFW model, the Einasto (1965) model, and an adiabatically compressed NFW model). We then determined the corresponding best fit that would be found using the two

standard H0LiCOW lens models: the power law model or the combination of the input de Vaucouleurs (1948) model with an NFW halo. From the difference between the true and model values of  $\kappa_E$  we can estimate the resulting fractional error in  $H_0$ . The typical scale of the systematic error in  $H_0$  is  $\sim 10\%$ . On the one hand, this seems remarkably good given the simplicity of the mass models. On the other hand, it also means that the accuracy of all current estimates of  $H_0$  from gravitational lens time delays is  $\sim 10\%$  independent of the reported precision of the measurement.

As emphasized by Schneider, & Sluse (2013), using mass models with additional degrees of freedom, so that determining  $R_E$  and  $\xi$  does not force a particular value of  $\kappa_E$  in our language, is the easiest way to ensure that the precision of the measurement does not exceed the accuracy even in the presence of very strong constraints from the lens data. The power law model should clearly simply be abandoned – while it is adequate for  $\sim 10\%$  estimates of  $H_0$  it is essentially useless if higher accuracies are needed. Combin-

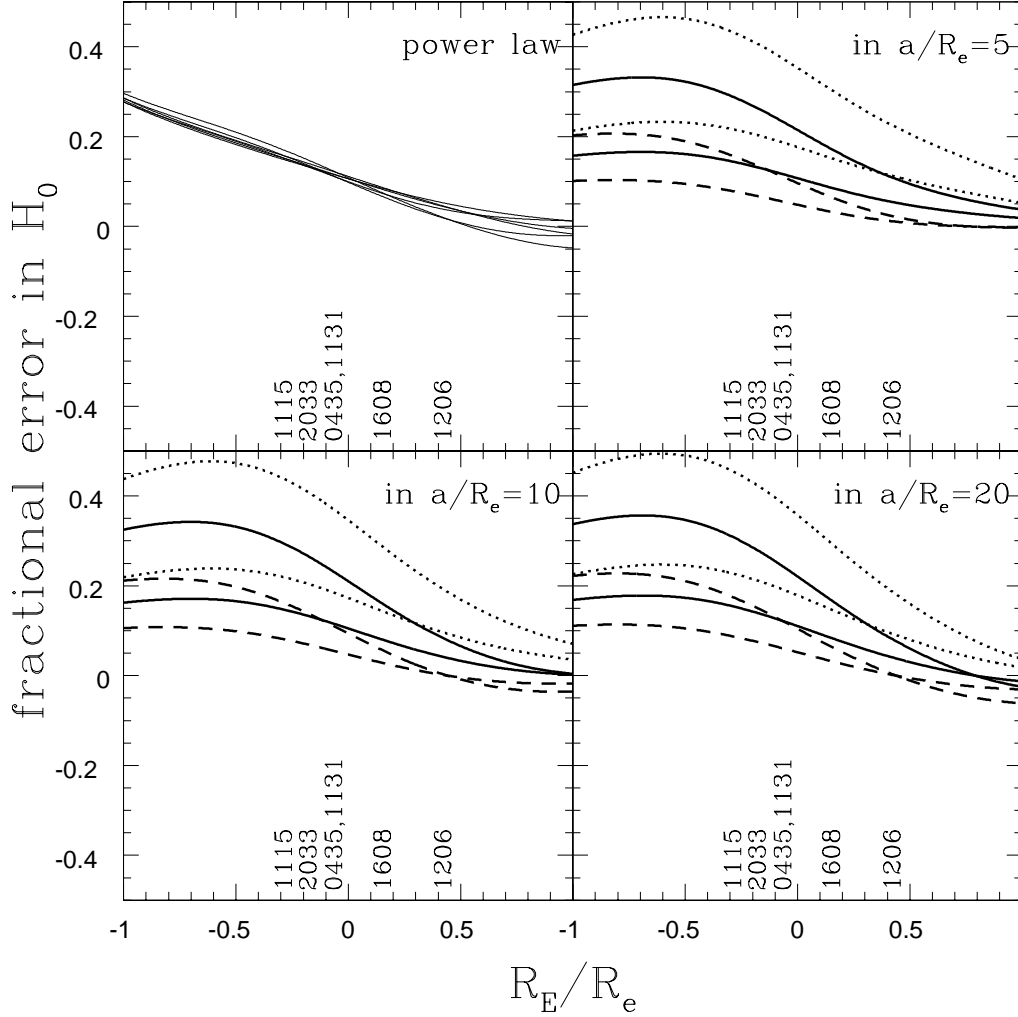


**Figure 7.** Fractional errors in  $H_0$  for adiabatically compressed NFW halos. The top left panel shows the results for the power law models and the other three panels are for the deV+NFW models where the input model has  $a/R_E = 5$  (top right), 10 (lower left) or 20 (lower right) and the lens model has  $a/R_E = 5$  (dashed), 10 (solid) or 20 (dotted). All panels include both the  $f_{DM} = 25\%$  and 50% cases.

ing the stellar distribution with an NFW model can capture much of this uncertainty if the scale radius of the NFW component is allowed a significant dynamic range. The current H0LiCOW models generally constrain the scale length to 10-15%, essentially making it a two parameter model like the power law models. Even to the extent that NFW models are correct, the scatter of lenses in mass and the spread of concentrations seen at fixed mass mean that the scale length should really be allowed to vary by a factor of  $\sim 2$ .

While we have emphasized the radial structure of the density distribution because it then allows us to carry out a large model survey, one should have similar concerns about the number of degrees of freedom in the angular structure. In our example from §2.2 of a lens producing a large fractional error in  $H_0$ , the problems only worsened when we considered a non-circular version of the same lens. The angular structure of the lens drove the models to have a radial density distribution with  $\kappa_E$  even more divergent from the true value than in the circular models. Models need to have

enough angular degrees of freedom that the angular structure beyond the quadrupole is not largely determined by the radial mass distribution of a single ellipsoidal density distribution (see Kochanek 2006).

There will remain a fundamental problem. While mass models with more degrees of freedom can capture the uncertainties in  $H_0$  created by the uncertainties in halo structure, these are largely systematic rather than random problems. For example, if halos were truly NFW models with a factor of two random scatter in the NFW scale length, then we might legitimately average the results from multiple lenses to produce a joint estimate of  $H_0$  with smaller uncertainties than for the individual lenses. However, if the freedom from allowing a broad range of scale lengths is really compensating for the fact that the real mass distribution is systematically different from the mean behavior of the model, then there is no reduction in the uncertainties from averaging multiple lenses.

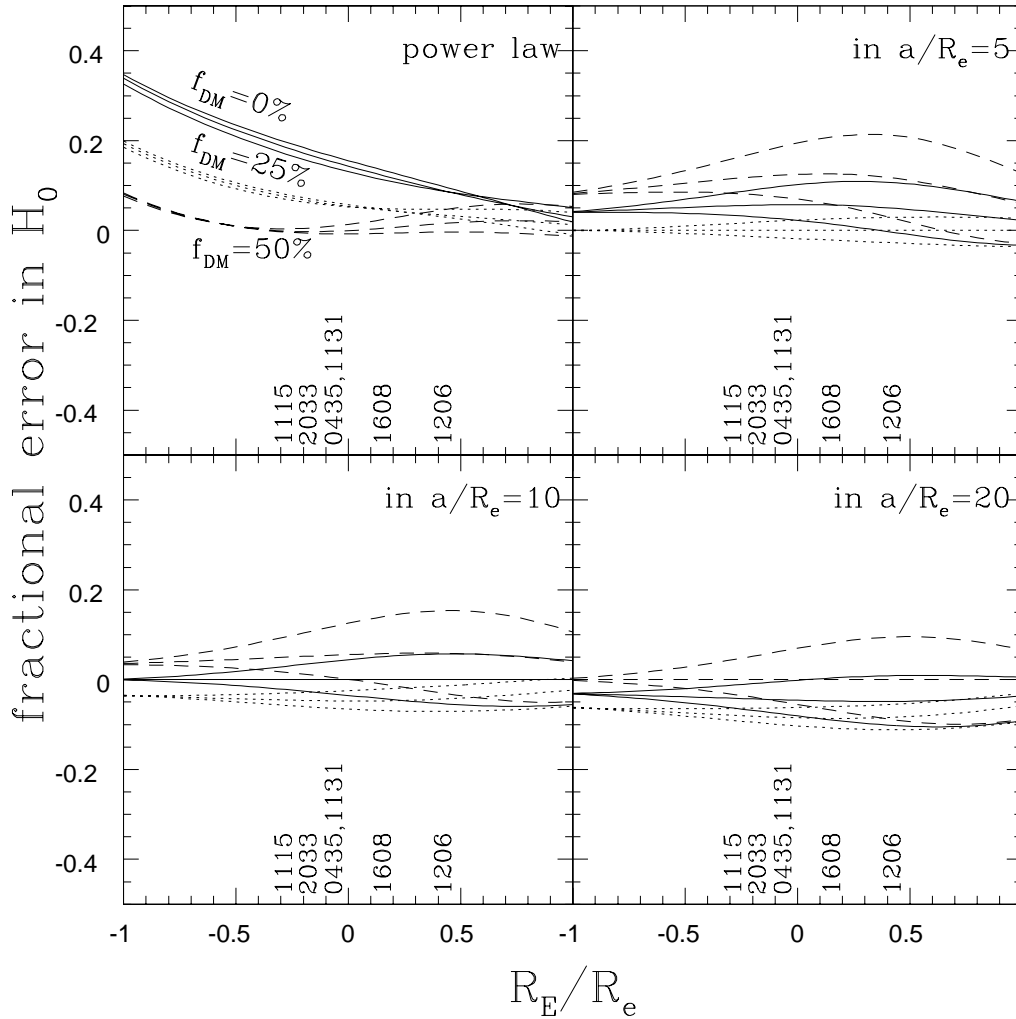


**Figure 8.** Fractional errors in  $H_0$  for models with mass-to-light ratio gradients. Results are shown for fractional changes per  $R_e$  of  $\mu = -0.2$  (top), 0 and 0.2 (bottom). The upper left panel for the power law models shows the cases with  $f_{DM} = 0\%$ , 25% and 50%. The other three panels are for the deV+NFW models where the input model has  $f_{DM} = 25\%$  and  $a/R_E = 5$  (top right), 10 (lower left) or 20 (lower right) and the lens model has  $a/R_E = 5$  (dashed), 10 (solid) or 20 (dotted). Generally the  $\mu = 0.2$  case is at the top and the  $\mu = -0.2$  case is at the bottom.

## ACKNOWLEDGMENTS

The author thanks the H0LiCOW collaboration for answering many questions, and C. Keeton for rapidly fixing a minor problem in `lensmodel`. CSK is supported by NSF grants AST-1908952 and AST-1814440.

## REFERENCES

- Agnello, A., Sonnenfeld, A., Suyu, S. H., et al. 2016, MNRAS, 458, 3830
- Auger, M. W., Treu, T., Bolton, A. S., et al. 2010, ApJ, 724, 511
- Birrer, S., Treu, T., Rusu, C. E., et al. 2019, MNRAS, 484, 4726
- Blumenthal, G. R., Faber, S. M., Flores, R., et al. 1986, ApJ, 301, 27
- Bolton, A. S., Brownstein, J. R., Kochanek, C. S., et al. 2012, ApJ, 757, 82
- Bonvin, V., Courbin, F., Suyu, S. H., et al. 2017, MNRAS, 465, 4914
- Bonvin, V., Millon, M., Chan, J. H. H., et al. 2019, arXiv e-prints, arXiv:1905.08260
- Bullock, J. S., Kolatt, T. S., Sigad, Y., et al. 2001, MNRAS, 321, 559
- Chen, G. C.-F., Fassnacht, C. D., Suyu, S. H., et al. 2019, arXiv e-prints, arXiv:1907.02533
- Courbin, F., Bonvin, V., Buckley-Geer, E., et al. 2018, AAP, 609, A71
- de Vaucouleurs, G. 1948, Annales d’Astrophysique, 11, 247
- Dutton, A. A., & Macciò, A. V. 2014, MNRAS, 441, 3359
- Einasto, J. 1965, Trudy Astrofizicheskogo Instituta Alma-Ata, 5, 87
- Gavazzi, R., Treu, T., Rhodes, J. D., et al. 2007, ApJ, 667, 176

- Gorenstein, M. V., Falco, E. E., & Shapiro, I. I. 1988, *ApJ*, 327, 693
- Grogin, N. A., & Narayan, R. 1996, *ApJ*, 464, 92
- Hernquist, L. 1990, *ApJ*, 356, 359
- Keeton, C. R. 2001, arXiv e-prints, astro-ph/0102340
- Keeton, C. R. 2011, GRAVLENS: Computational Methods for Gravitational Lensing, ascl:1102.003
- Kochanek, C. S. 2002, *ApJ*, 578, 25
- Kochanek, C. S. 2006, Saas-fee Advanced Course 33: Gravitational Lensing: Strong, Weak and Micro, 91
- Koopmans, L. V. E., Bolton, A., Treu, T., et al. 2009, *ApJL*, 703, L51
- Kormendy, J., & Djorgovski, S. 1989, *ARA&A*, 27, 235
- Kundić, T., Turner, E. L., Colley, W. N., et al. 1997, *ApJ*, 482, 75
- Liao, K., Treu, T., Marshall, P., et al. 2015, *ApJ*, 800, 11
- Merritt, D., Navarro, J. F., Ludlow, A., et al. 2005, *ApJL*, 624, L85
- Moore, B., Quinn, T., Governato, F., et al. 1999, *MNRAS*, 310, 1147
- Muñoz, J. A., Kochanek, C. S., & Keeton, C. R. 2001, *ApJ*, 558, 657
- Navarro, J. F., Frenk, C. S., & White, S. D. M. 1997, *ApJ*, 490, 493
- Navarro, J. F., Ludlow, A., Springel, V., et al. 2010, *MNRAS*, 402, 21
- Planck Collaboration, Aghanim, N., Akrami, Y., et al. 2018, arXiv e-prints, arXiv:1807.06209
- Press, W. H., Rybicki, G. B., & Hewitt, J. N. 1992, *ApJ*, 385, 404
- Reed, D. S., Koushiappas, S. M., & Gao, L. 2011, *MNRAS*, 415, 3177
- Refsdal, S. 1964, *MNRAS*, 128, 307
- Romanowsky, A. J., & Kochanek, C. S. 1999, *ApJ*, 516, 18
- Rusin, D., & Kochanek, C. S. 2005, *ApJ*, 623, 666
- Rusu, C. E., Wong, K. C., Bonvin, V., et al. 2019, arXiv e-prints, arXiv:1905.09338
- Schild, R. E. 1990, *AJ*, 100, 1771
- Schneider, P., & Sluse, D. 2013, *AAP*, 559, A37
- Sersic, J. L. 1968, Cordoba
- Sonnenfeld, A. 2018, *MNRAS*, 474, 4648
- Suyu, S. H., Marshall, P. J., Auger, M. W., et al. 2010, *ApJ*, 711, 201
- Suyu, S. H., Auger, M. W., Hilbert, S., et al. 2013, *ApJ*, 766, 70
- Tonry, J. L. 1998, *AJ*, 115, 1
- Treu, T., & Koopmans, L. V. E. 2002, *MNRAS*, 337, L6
- Unruh, S., Schneider, P., & Sluse, D. 2017, *AAP*, 601, A77
- Walsh, D., Carswell, R. F., & Weymann, R. J. 1979, *Nature*, 279, 381
- Wertz, O., Orthen, B., & Schneider, P. 2018, *AAP*, 617, A140
- Wong, K. C., Suyu, S. H., Auger, M. W., et al. 2017, *MNRAS*, 465, 4895
- Wong, K. C., Suyu, S. H., Chen, G. C.-F., et al. 2019, arXiv e-prints, arXiv:1907.04869
- Xu, D., Sluse, D., Schneider, P., et al. 2016, *MNRAS*, 456, 739